

See discussions, stats, and author profiles for this publication at: <https://www.researchgate.net/publication/231229295>

Lower Incorporation of Impurities in Ferritin Crystals by Suppression of Convection: Modeling Results

ARTICLE *in* CRYSTAL GROWTH & DESIGN · NOVEMBER 2000

Impact Factor: 4.89 · DOI: 10.1021/cg005515g

CITATIONS

35

READS

18

5 AUTHORS, INCLUDING:



Hong Lin

Ocean University of China

214 PUBLICATIONS 3,640 CITATIONS

SEE PROFILE



Dimitar Petsev

University of New Mexico

97 PUBLICATIONS 2,784 CITATIONS

SEE PROFILE



S.s.-T. Yau

University of Illinois at Chicago

134 PUBLICATIONS 2,451 CITATIONS

SEE PROFILE



Peter G Vekilov

University of Houston

168 PUBLICATIONS 5,647 CITATIONS

SEE PROFILE

Lower Incorporation of Impurities in Ferritin Crystals by Suppression of Convection: Modeling Results

Hong Lin,[†] Dimiter N. Petsev,[†] S.-T. Yau,[†] Bill R. Thomas,^{†,‡} and Peter G. Vekilov^{*,†,§}

Center for Microgravity and Materials Research and Department of Chemistry, University of Alabama in Huntsville, Huntsville, Alabama 35899, and Universities Space Research Association, Marshall Space Flight Center, Huntsville, Alabama 35875

Received September 6, 2000

ABSTRACT: We have developed an axi-symmetric time-dependent numerical model of the diffusive-convective transport of a crystallizing protein and an impurity, in an isothermal crystal growth system *at standard and zero gravity*. We model crystallization of ferritin, a protein with $M_w = 440\,000$, and its most abundant impurity, the protein's native dimer. The diffusivities of the protein and the dimer and the kinetic coefficients for crystallization and impurity incorporation are available. The model assumes the geometry of a cylindrical vessel used in protein crystallization trials on earth and in space, the DCAM. At terrestrial gravity, buoyancy-driven convection with a maximum velocity of $12\ \mu\text{m/s}$ enhances the supply of both protein and impurity. In the absence of convection, e.g., at $0g$, the diffusion depletion zone is wider and the interfacial concentrations drop significantly. The lower diffusivity of the larger dimer results in its incorporation at $0g$ lower by factors of 2–3 than on earth. The three-dimensional computational scheme used here allows direct comparisons of these results with space and laboratory experimental data. The two data sets agree quantitatively, suggesting that in some cases the improved quality of space-grown crystals as compared to the earth-grown controls may be due to the suppressed supply of larger impurities.

1. Introduction

Protein crystallography is still the dominant method for determination of the atomic structures of the protein molecules.¹ The production of high-quality crystals of many proteins with important biological functions is often a major hurdle in structure studies.² Incorporation of impurities, which can be other proteins or macromolecules or modifications of the native protein, has been identified as a major factor of protein crystal imperfection.^{3–5} In many cases, the impurity species responsible for the deterioration of the crystal quality have been identified as nondissociable aggregates (oligomers, clusters) of native protein molecules.^{6–10}

During growth, the protein in the solution layer around a crystal is depleted and the solution density decreases.^{11,12} In the presence of gravity, density gradients give rise to convective flows of the solution. Such flows may affect the growth processes that have characteristic length scales comparable to the transport length scales and lead to defects in the crystal.^{13,14} Furthermore, the convective flows enhance the supply of impurity molecules to the interface. If the impurities are preferentially incorporated into the crystals, convective flows may increase the impurity incorporation, increase the concentration of the impurity-related defects, and lower the crystals' quality and utility.

Suppression of impurity supply via convection has been put forth as an explanation of the improved quality of crystals grown under conditions that suppress or eliminate convection: in microgravity^{2,10,15,16} or in solutions whose viscosity is increased by a gelating agent.¹⁷

A counterargument states the slower crystal growth under pure diffusion control leads to increased exposure times of the interstep terraces, which may lead to enhanced impurity incorporation and balance the benefit from slower impurity supply.¹⁸ Direct tests comparing the impurity supply fields in the presence and absence of convection have not been carried out: quantifications of impurity distributions on the background of nonuniform main protein field may require unique and heavy experimental equipment.¹⁹

Hence, the goal of the studies reported here is to numerically model the coupled solutal transport and incorporation of the main protein and an impurity species into a growing protein crystal.^{12,20,21} We compare two sets of conditions, conducive either of convective–diffusive transport driven by terrestrial gravity or of purely diffusive transport. The latter case may involve, for instance, the absence of gravity on board of spacecraft. We simulate the crystallization of ferritin, a major iron storage protein in the cytosol.^{22,23} The major contaminant in ferritin preparations is its molecular dimer, whose concentration can be brought down by biochemical purification techniques to as low as $\sim 5\%$ (w/v).⁸ However, as Figure 1 illustrates, even at these relatively low bulk concentrations, the dimer species (for identification and characterization of the dimer, see ref 24) adsorbs at the interface. The surface dimer concentration from Figure 1 is ~ 20 molecules/ μm^2 , and this is 2–3 orders of magnitude higher than the value in a 10 nm thick layer containing solution with the above bulk concentration.²⁵ During growth, most of the dimers are incorporated by the growing crystal layers and cause point defects, lattice strain, and mosaicity.^{25,26} We will test if the suppression of convective supply of solute and impurities may result in lower incorporation of dimers. The predicted levels of impurity trapping will be com-

[†] Center for Microgravity and Materials Research, University of Alabama at Huntsville.

[‡] Marshall Space Flight Center.

[§] Department of Chemistry, University of Alabama at Huntsville.

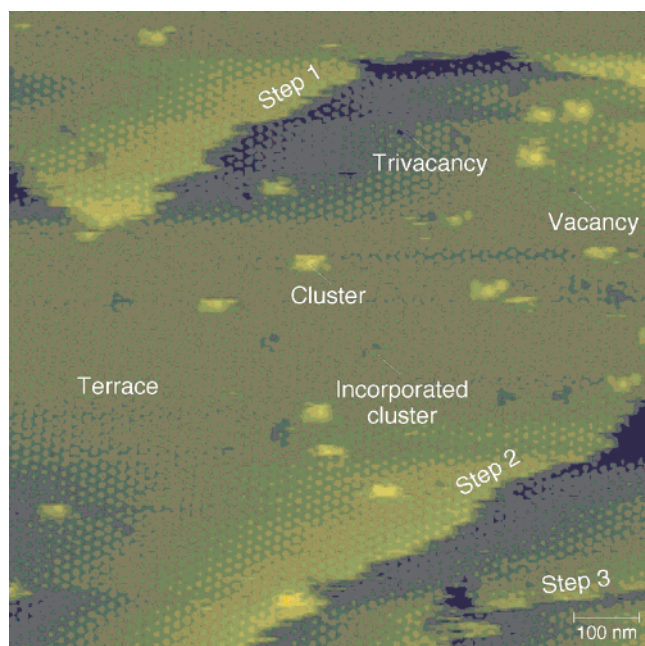


Figure 1. In situ atomic force microscopy image of the growing crystal surface: growth steps with adsorbed impurity clusters and related point defects on the terraces between the steps.

pared to published results from ferritin crystallization experiments carried out on board the space shuttle and their laboratory controls.¹⁰

2. Model Description

2.1. Geometry and Basic Assumptions. We assume the geometry of a vessel often used in protein crystallization trials on earth and in space, the diffusion-controlled crystallization apparatus for microgravity (DCAM).²⁷ Meaningful comparisons between computational predictions of impurity incorporation and corresponding experimental data require a three-dimensional model of the bulk transport processes: two-dimensional models exaggerate the ratio of the surface of the crystal to the solution volume and predict solution depletion faster than actual.¹² To shorten the processor time required for the computations, we assume cylindrical symmetry of the model system. This assumption is adequate to the modeled vessel, and we do not believe that assuming a cylindrical crystal shape would introduce any significant bias in the model results. Furthermore, an investigation of the role of convective supply of impurities does not require a detailed model of the kinetics of growth layers on the solution–crystal interface, in contrast to our previous work.^{21,28,29} This allows us to assume that the face growth rate is proportional to the supersaturation at the interface. To preserve the faceting of the crystal throughout a model run, we assume a uniform growth rate of the horizontal and vertical crystal faces, governed by the supersaturation at the crystal's edge. Through this assumption, we implicitly account for the layer growth mode of the protein crystals.²¹

The growth cell is represented by a cylinder with height and radius set at the respective DCAM values: 10.75 and 8.75 mm (see Figure 2a). We assume that the crystal has a cylindrical shape with a height of 250 μm

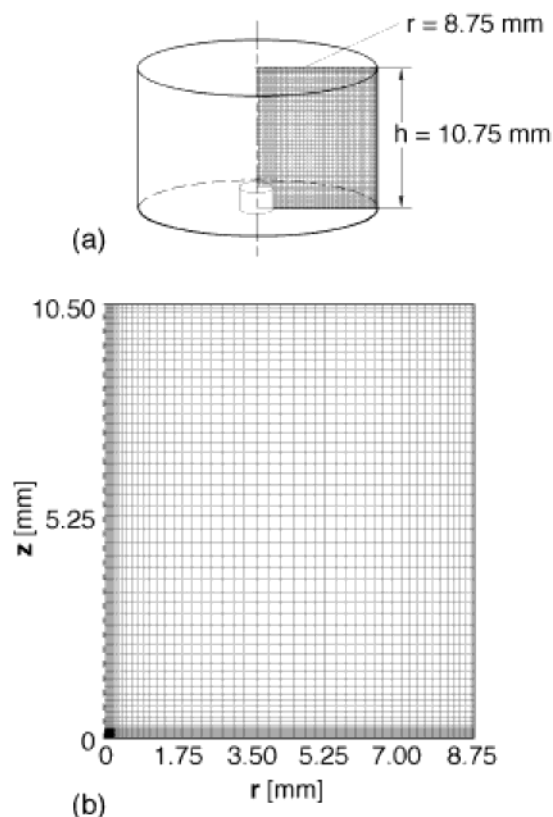


Figure 2. Geometry and grid used in the simulation: (a) model geometry same as the diffusion-controlled crystallization apparatus for microgravity (DCAM); (b) variable-density mesh used in the simulations.

and a diameter of 500 μm . As depicted in Figure 2a, the crystal rests in the center of the bottom of the cell. Besides ferritin, the solution contains solvent: water, sodium acetate buffer, and CdSO_4 precipitant. In the transport simulations, the solvent is assumed to act as an inert medium. The temperature in the whole cell is assumed to be constant and uniform throughout the growth process. Hence, only compositional nonuniformities evolve in the solution due to the crystallization process. Since the local mass density of the solution depends on the protein concentration at the respective point, these nonuniformities are a source for buoyancy-driven convection. The growth rate is very low; hence, it is admissible to fix the crystal size during the calculation.

2.2. Governing Equations. The nonsteady transport of mass, momentum, and dissolved protein molecules (monomers and dimers) is governed by the following equations in dimensionless form indicated by the tilde over the variable symbol. Length-related variables and parameters were scaled by the crystal height, h_c , while h_c^2/ν was used for scaling time; ν is the kinematic viscosity. The velocities were scaled by ν/h_c , the pressure by $\rho\nu^2/h_c^2$ (with ρ being density, see below), and the mass concentration of protein by $C_{A,0} - C_{A,\text{eq}}$, where $C_{A,0}$ is the initial ferritin concentration and $C_{A,\text{eq}}$ is the concentration of equilibrium with the crystals.

Assuming cylindrical symmetry, and using

$$\rho = \bar{\rho}_{\text{salt}} + \beta C_A, \quad \beta = \frac{\partial \rho}{\partial C_A} \quad (1)$$

where ρ is the solution mass density, $\bar{\rho}_{\text{salt}}$ is the density

of the solvent including the dissolved electrolyte, and β (which is dimensionless) is the density increment with monomer protein concentration C_A , we write the continuity equation in cylindrical coordinates (r, z)

$$\frac{\beta}{\tilde{\rho}} \left(\frac{\partial \tilde{C}_A}{\partial \tilde{t}} + \tilde{u}_r \frac{\partial \tilde{C}_A}{\partial \tilde{r}} + \tilde{u}_z \frac{\partial \tilde{C}_A}{\partial \tilde{z}} \right) + \frac{\tilde{u}_r}{\tilde{r}} + \frac{\partial \tilde{u}_r}{\partial \tilde{r}} + \frac{\partial \tilde{u}_z}{\partial \tilde{z}} = 0 \quad (2)$$

Here \mathbf{u} is the solution velocity vector. For low concentrations of protein, $\beta/\tilde{\rho} \ll 1$, the first three terms in the left-hand side of eq 2 can be ignored and we obtain

$$\frac{\tilde{u}_r}{\tilde{r}} + \frac{\partial \tilde{u}_r}{\partial \tilde{r}} + \frac{\partial \tilde{u}_z}{\partial \tilde{z}} = 0 \quad (3)$$

The momentum balance, in the Boussinesq approximation, reads

$$\frac{\partial \tilde{u}_r}{\partial \tilde{t}} + \tilde{u}_r \frac{\partial \tilde{u}_r}{\partial \tilde{r}} + \tilde{u}_z \frac{\partial \tilde{u}_r}{\partial \tilde{z}} = \frac{\partial \tilde{p}}{\partial \tilde{r}} + \frac{\partial}{\partial \tilde{r}} \left(\frac{1}{\tilde{r}} \frac{\partial}{\partial \tilde{r}} (\tilde{r} \tilde{u}_r) \right) + \frac{\partial^2 \tilde{u}_r}{\partial \tilde{z}^2} \quad (4)$$

$$\frac{\partial \tilde{u}_z}{\partial \tilde{t}} + \tilde{u}_r \frac{\partial \tilde{u}_z}{\partial \tilde{r}} + \tilde{u}_z \frac{\partial \tilde{u}_z}{\partial \tilde{z}} = \frac{\partial \tilde{p}}{\partial \tilde{z}} + \frac{1}{\tilde{r}} \frac{\partial}{\partial \tilde{r}} \left(\tilde{r} \frac{\partial \tilde{u}_z}{\partial \tilde{r}} \right) + \frac{\partial^2 \tilde{u}_z}{\partial \tilde{z}^2} + \frac{\text{Ra}}{\text{Sch}} \tilde{C}_A \tilde{g}_z \quad (5)$$

The last term in eq 5 is not present in (4), since we assume strictly vertical orientation of the cell axis, in which the component of the gravity vector along the horizontal coordinate $g_r = 0$. The convective diffusion of the main protein species and the impurities is governed by

$$\frac{\partial \tilde{C}_A}{\partial \tilde{t}} + \tilde{u}_r \frac{\partial \tilde{C}_A}{\partial \tilde{r}} + \tilde{u}_z \frac{\partial \tilde{C}_A}{\partial \tilde{z}} = \frac{1}{\text{Sch}} \left[\frac{1}{\tilde{r}} \frac{\partial}{\partial \tilde{r}} \left(\tilde{r} \frac{\partial \tilde{C}_A}{\partial \tilde{r}} \right) + \frac{\partial^2 \tilde{C}_A}{\partial \tilde{z}^2} \right] \quad (6)$$

The dimensionless protein concentration in eq 6 is defined by $\tilde{C}_A = C_A/(C_{A,0} - C_{A,\text{eq}})$. The respective Rayleigh and Schmidt numbers are

$$\text{Ra} = \frac{\beta h_c^3 g_z (C_{A,0} - C_{A,\text{eq}})}{\rho_{\text{in}} \nu D_A} \quad \text{Sch} = \nu/D_A \quad (7)$$

where D_A is the protein diffusivity and ρ_{in} is the initial mass density of the solution.

2.3. Initial and Boundary Conditions. At the initial moment the solution is at rest and the concentrations of all components are uniform throughout the whole volume, i.e.

$$\tilde{u}_r = 0, \quad \tilde{u}_z = 0, \quad \tilde{C}_A = 1 \quad (8)$$

No-slip hydrodynamic conditions and component impermeability are applied to the cell wall:

$$\tilde{u}_r = 0, \quad \tilde{u}_z = 0 \quad (9)$$

and

$$\nabla \tilde{C} \cdot \mathbf{n}_w = 0 \quad (10)$$

where \mathbf{n}_w is the normal unit vector.

The interface mass balance yields (i) at top of the crystal

$$\tilde{u}_z = -\tilde{R} \left(1 - \frac{\rho_c}{\rho} \right) \quad (11)$$

and (ii) on the side of the crystal

$$\tilde{u}_r = -\tilde{R} \left(1 - \frac{\rho_c}{\rho} \right) \quad (12)$$

where R is the normal growth rate of the crystal obtained from

$$\tilde{R} = b\tilde{\sigma} \quad (13)$$

Here, b is the face kinetic coefficient, $\tilde{\sigma} = (C_A - C_{\text{eq}})/C_{\text{eq}}$ is the supersaturation, and ρ and ρ_c are, respectively, the solution and crystal mass density.

The boundary condition for the ferritin concentration at the crystal interface is

$$\frac{\partial \tilde{C}_A}{\partial \tilde{x}_i} - \frac{\tilde{R} \rho_c \nu}{D_A} = 0 \quad \tilde{x}_i = \tilde{r}, \tilde{z} \quad (14)$$

while the condition for the dimer segregation is

$$\frac{\partial \tilde{C}_{\text{dimer}}}{\partial \tilde{x}_i} - \frac{\tilde{R} K_s \nu}{D_{\text{dimer}}} \left(\frac{C_{A,\text{crystal}}}{C_{A,\text{solution}}} \right) \tilde{C}_{\text{dimer}} = 0 \quad (15)$$

In eq 15 K_s is the segregation coefficient at the crystal-solution interface defined as

$$K_s = \frac{(C_{\text{dimer}}/C_{\text{monomer}})_{\text{crystal}}}{(C_{\text{dimer}}/C_{\text{monomer}})_{\text{solution}}} \quad (16)$$

In Section 4 we compare the segregation of dimer resulting from these simulation to experimental results. For the experimental determinations of the segregation coefficient, the variables in the numerator of eq 16 are obtained by dissolving large crystals. Hence, the obtained values are averaged over the whole crystal. For a meaningful comparison with the model results, we define an averaged model segregation coefficient K_{eff} and calculate it in the following fashion:

$$K_{\text{eff}} = \frac{\langle (C_{\text{dimer}}/C_{\text{monomer}})_{\text{crystal}} \rangle}{(C_{\text{dimer}}/C_{\text{monomer}})_{\text{solution}}} \quad (17)$$

The ratio of $C_{\text{dimer}}/C_{\text{monomer}}$ in the crystal varies in time and is calculated through the respective fluxes at the interface

$$\left(\frac{C_{\text{dimer}}}{C_{\text{monomer}}} \right)_{\text{crystal}} = \frac{j_{\text{dimer}}}{j_{\text{monomer}}} \quad (18)$$

To obtain the averaged $\langle (C_{\text{dimer}}/C_{\text{monomer}})_{\text{crystal}} \rangle$ value, we integrated j_{dimer} and j_{monomer} over time and the whole crystal surface.

We assumed that the ratio $(C_{\text{dimer}}/C_{\text{monomer}})_{\text{solution}}$ does not change throughout a run in the relatively large crystallization cell, and we used

$$(C_{\text{dimer}}/C_{\text{monomer}})_{\text{solution}} = [(C_{\text{dimer}}/C_{\text{monomer}})_{\text{solution}}]_{\text{initial}} = 0.05 \quad (19)$$

The mesh used for the numerical calculation contains 61×55 gridlines with variable density that is finer

around the crystal and close to the boundary and is shown in Figure 2b. The discretization and numerical schemes used here are the same as in our previous paper.¹²

3. Experimental Determination of the Governing Parameters

The *diffusion coefficients* of monomers and dimers of ferritin were determined by dynamic light scattering (DLS) as described in ref 24. The obtained values are: for the monomer $D_A = 3.2 \times 10^{-7} \text{ cm}^2/\text{s}$, and for the ferritin dimer $2.2 \times 10^{-7} \text{ cm}^2/\text{s}$.

The *density increment with protein concentration* β is defined by eq 1, and with ϕ_F being the ferritin volume fraction in the solution

$$\begin{aligned}\bar{\rho} &= \rho_{\text{salt}} + (\rho_F - \rho_{\text{salt}})\phi_F \\ &= \rho_{\text{salt}} + (\rho_F - \rho_{\text{salt}})\frac{4\pi a_F^3 N_A}{3M_W}C_A\end{aligned}\quad (20)$$

is the average density of the protein solution as a function of its mass concentration (in g/mL). ρ_{salt} is the density of the solvent in absence of protein, and ρ_F is the density of the protein molecule. The constants N_A , M_W and a_F^3 are respectively the Avogadro number and the ferritin molecular mass and volume, a_F being an effective molecular size. Assuming that the pure ferritin density, ρ_F , does not change with the concentration we may write

$$(\rho_F - \rho_{\text{salt}})\frac{4\pi a_F^3 N_A}{3M_W} = \frac{\partial \bar{\rho}}{\partial C_A}\quad (21)$$

Since the ferritin crystals contains trapped water, the ferritin density, ρ_F , cannot be extracted from the crystal density. However, we can determine $\partial \bar{\rho} / \partial C_A$ by measuring the density of the background solvent, ρ_{salt} , and the protein solution density $\bar{\rho}$ at known concentration, C_A . With these, using (20) and (21), we get

$$\frac{\partial \bar{\rho}}{\partial C_A} = \frac{\bar{\rho} - \rho_{\text{salt}}}{C_A}\quad (22)$$

The above equation is used to determine the derivative $\partial \bar{\rho} / \partial C_A$. Accurately measured volumes (5 mL) of background and protein solutions were weighted on a Mettler A200 balance. Then the difference between the two solutions was divided by the ferritin concentration, C_A . The accuracy of the measurement increases with the concentration, which in our particular case was $C_A = 0.02 \text{ g/mL}$. Following this methodology, we obtain $\partial \bar{\rho} / \partial C_A = 0.28$.

The *face kinetic coefficient* b , defined by eq 13, is linked to the step kinetic coefficient β_{step} as

$$b = \beta_{\text{step}} \Omega C_{\text{eq}} p\quad (23)$$

where Ω is the crystal volume per molecule; for the fcc apoferritin crystals with a lattice constant $c = 18.4 \text{ nm}$,^{30,31} $\Omega = 1/4c^3 = 1.56 \times 10^{-18} \text{ cm}^3$, and $\Omega C_e = 5 \times 10^{-5}$. The variable p is the average vicinal slope of the surface, proportional to step density,^{32,33} and at the high supersaturation at which ferritin crystals are typically

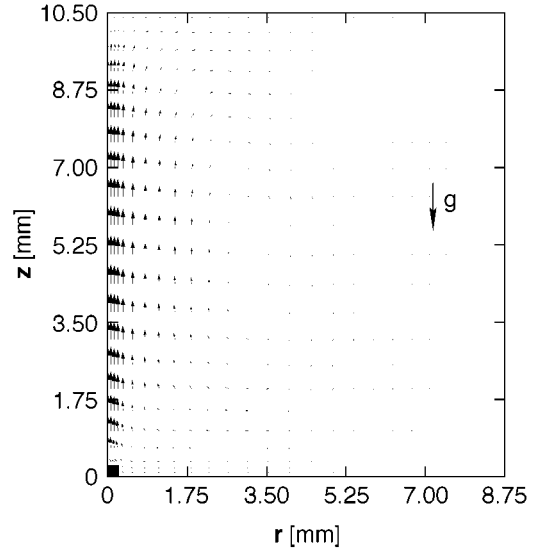


Figure 3. Solution velocity field after 1 h of growth at $g = 1$. The maximum velocity reached is $12 \mu\text{m/s}$.

grown, $p = 2 \times 10^{-2}$.³⁶ With $\beta_{\text{step}} = 2.5 \times 10^{-4} \text{ cm/s}$,³⁶ $b = 2.5 \times 10^{-10} \text{ cm/s}$.

The experimentally determined *impurity segregation coefficient* K for crystals grown under terrestrial gravity conditions, i.e., when buoyancy-driven convective stirring is present, vary between 3 and 4.³⁷ Since even on earth a layer depleted with respect to proteins and impurity exists, we set $K_s = 8$.

We assume the typical crystallization conditions for ferritin. The *initial concentration* of monomer protein molecules is 1.0 mg/mL . Ferritin *dimers* are present at 0.05 mg/mL .^{8,10} The initial *solution mass density* is $\rho = 1.03 \text{ g/cm}^3$.

4. Results and Discussion

4.1. Convective–Diffusive Transport at $g = 1$. As a ferritin crystal grows, the protein in the solution layer around it is depleted and the solution density decreases. In the presence of gravity this lower density solution rises and is replaced by portions of solution of higher protein concentration coming from the side. This leads to the gradual development of a typical convection roll that pumps fresh solution toward the growing crystal. Figure 3 shows the convection velocity field, which develops after 1 h of growth. At this time, the maximum convection velocity is $\sim 12 \mu\text{m/s}$ and this value is reached above the crystal, at about three-fourths of the total cell height. At a later point, the front of the convection roll spreads further along the periphery of the cell top. The value and the location of the maximum convection velocity do not change much.

The time evolution of the monomer concentration fields at times earlier than the one in Figure 3 is presented in Figures 4a–c. The solution concentration reaches 99% of the value far from the crystal at only $\sim 0.3 \text{ mm}$ from the crystal surface, and this distance does not change with time; i.e., the convection strongly enhances the transport of higher concentration solution from the periphery of the container to the crystal. Furthermore, the concentration at the center of the top crystal face is $\sim 40\%$ of the bulk concentration, while at the crystal edge, it is $\sim 70\text{--}80\%$ of the bulk. This strong

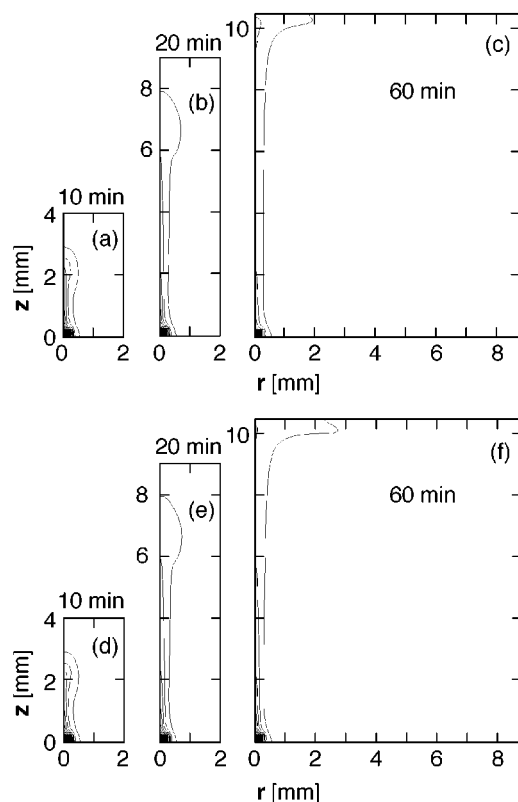


Figure 4. Concentration contours after times of growth indicated on each panel at $g = 1$: (a–c) concentration fields of ferritin monomer; (d–f) concentration fields of ferritin dimer. In all panels, the outermost contour corresponds to concentration 99% of the initial and the second contour to 90%; the spacing between the other isoconcentration contour lines equals 10% of the monomer or dimer concentration in the bulk.

nonuniformity of the solute concentration along the crystal face depends on the crystal size. At crystal sizes larger than $\sim 200 \mu\text{m}$, the concentration at the face center is so much lower than at the edge that new crystal layers are preferentially nucleated at the edges; at smaller sizes, layers are uniformly nucleated along the whole face.³⁸ This behavior of the ferritin system is similar to previously studied lysozyme crystal growth.^{21,34,35}

The evolution of the dimer concentration field is shown in Figure 4d–f. The concentration fields for monomers and dimers look qualitatively alike; however, due to the lower diffusivity (see section 3), the dimer concentration fields are somewhat wider than those of the monomers. A solution with higher dimer concentration is brought by the convective flow to $\sim 0.5 \text{ mm}$ from the crystal surface. The lower diffusivity of the dimer contributes to dimer concentration nonuniformity over the top face stronger than that of the monomer. As with lysozyme, nonuniform impurity concentration over a face may be a factor that determines the morphology in some growth situations.^{15,21,34,35}

4.2. Diffusive Supply of Monomers and Dimers at $g = 0$. In absence of gravity ($\tilde{g} = 0$) there are no convective flows in the cell, and this is reflected in the Navier–Stokes equations (4) and (5). The diffusion field around the crystal attains semispherical symmetry. In time, the depleted area slowly spreads toward to container walls. Comparing the outermost 99% contour in

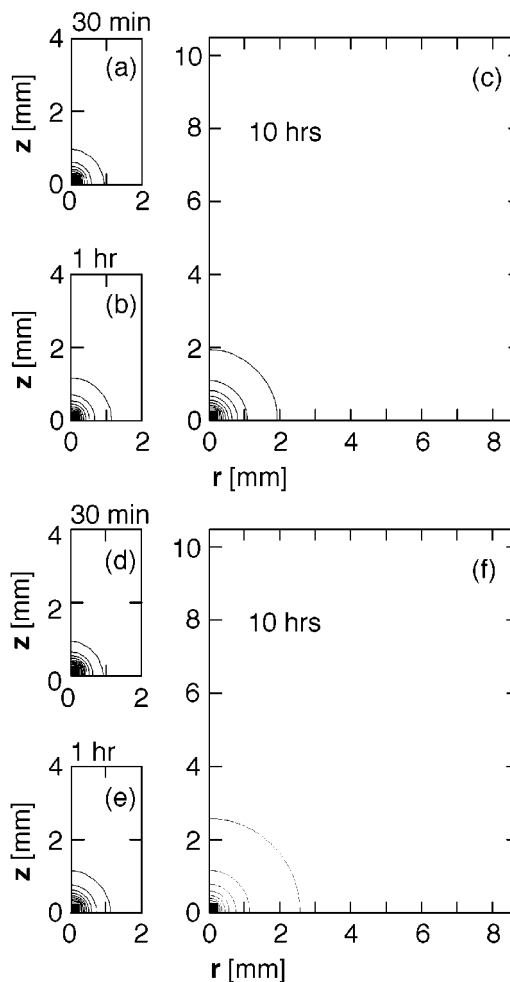


Figure 5. Concentration contours after times of growth indicated on each panel at $g = 0$: (a–c) concentration fields of ferritin monomer; (d–f) concentration fields of ferritin dimer. In all panels, the outermost contour corresponds to concentration 99% of the initial and the second contour to 90%; the spacing between the other isoconcentration contour lines equals 10% of the monomer or dimer concentration in the bulk.

Figures 5a–c, we can extract a rate of diffusion of $\sim 0.05 \mu\text{m/s}$, significantly lower than the convection velocity present in the earth's gravity field. The slow rate of diffusion makes it necessary to run the diffusive transport computations for longer times. Still, even after 10 h of simulated growth, the depleted solution layer is far from the container walls. The monomer concentration at the top face edge, $\sim 50\%$ of the initial, is lower than in the case of convective–diffusive supply. The concentration nonuniformity over the top crystal face is also lower than in the previous case, with the value at the facet center being $\sim 40\text{--}45\%$ of the initial protein concentration.

Comparing Figure 5c,f to Figure 4c,f, we find that the dimer supply field follows the geometry of the monomer distribution significantly better than in the convective–diffusive case. Because of the lower dimer diffusivity, the dimer supply fields are wider, and the dimer concentration at the interface is even lower than in the case represented in Figure 4. Furthermore, the nonuniformity of the dimer concentration over the top face is about the same as that of the monomer at 5–10%.

4.3. Convection Effects on Dimer Segregation and Incorporation. The comparison between mono-

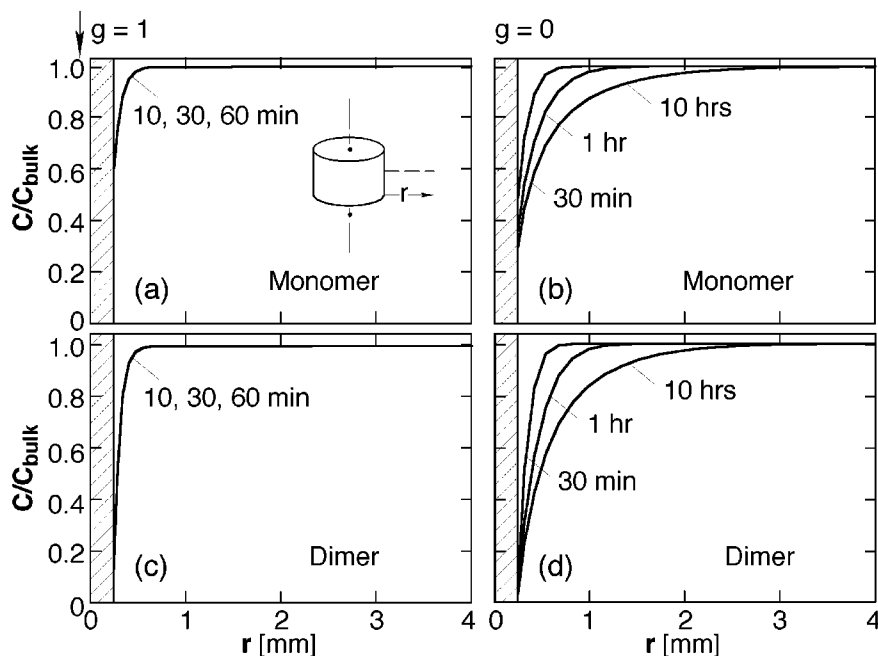


Figure 6. Concentration profiles along horizontal dashed line in insert in (a). The hatched area on the left of each panel represents the crystal. Times are indicated on the plots. Panels a and b are for ferritin monomer and panels c and d for ferritin dimer. Results are given for simulations assuming $g = 1$ for panels a and c and $g = 0$ for panels b and d.

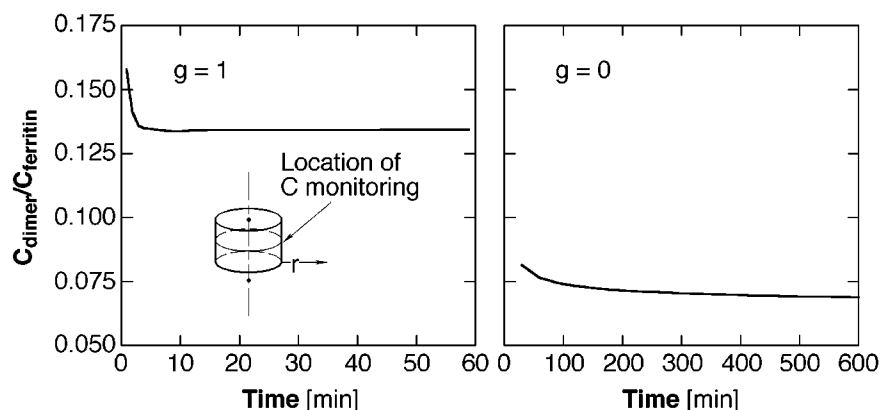


Figure 7. Variations of $C_{\text{dimer}}/C_{\text{monomer}}$ with time at a point on the crystal surface indicate in the insert. Results are given for simulations assuming $g = 1$ and $g = 0$. These curves are used toward the calculation of K_{eff} defined by eq 17.

mer and dimer supply fields in the cases of convective–diffusive and purely diffusive transport is summarized in Figure 6. It shows the concentration profiles for the two protein species along a line at $125 \mu\text{m}$ from the container bottom at three growth times for each transport mode. Figure 6a,c shows that the monomer and the dimer distributions reach a quasi-steady state after only 10 min of growth in the presence of buoyancy-driven convection and do not perceptibly change thereafter.

The concentration profiles in the absence of convection in Figure 6b,d do not reach steady or quasi-steady state. From these figures, we can evaluate an approximate maximum mass transport velocity for the case of purely diffusive supply. Note that because of the asymmetry of the convection field, the profiles in Figure 6a,c cannot be used for a similar evaluation; the value resulting from the solution of the Navier–Stokes equations of $12 \mu\text{m/s}$ was discussed in relation with Figure 4. The first curve in Figure 6b shows the depletion reaching about 0.6 mm for 30 min, resulting in a mass transport rate of $0.3 \mu\text{m/s}$.

More importantly for the purposes of this investigation, the suppression of convection reduces the interfacial concentration of the monomer by a factor of about 2—from 60% of the initial bulk concentration to $\sim 30\%$ in the 10 h profile (compare parts a and c of Figure 6). The corresponding reduction of the interfacial concentration of the dimer is about 4-fold from $\sim 15\%$ in Figure 6b to $\sim 3\text{--}4\%$ in Figure 6d. Since in eqs 13 and 16 we assumed that both crystal growth rate and impurity incorporation are proportional to the interfacial concentrations of, respectively, the monomer and dimer, we should expect 2-fold reduction in the amount of incorporated impurity if convection is suppressed.

The variations of the ratio of the concentrations of the monomer and the dimer entering the crystal at the surface location corresponding to the profiles in Figure 6, calculated using eq 18, are shown in Figure 7 for the two cases of transport. We see that, at almost all times, suppression of convection results in about 2-fold reduction of the incorporation of the impurity species in the crystal. Note that this is not a trivial conclusion.

Table 1. Comparisons of Effective Segregation Coefficient K_{eff} Resulting from Simulations and Experiments on Earth and in Space^a

	earth ($\bar{g} = 1$)	space ($\bar{g} = 0$)
exptl	3–4	1.5
simulation	2.9	1.5

^a Experimental data are taken from ref 10.

Buoyancy-driven convection at $g = 1$ does not ensure perfect mixing. Hence, the interfacial concentrations of protein and the impurity are not equal to those in the solution bulk; the depletion with respect to these two species is different, and both interfacial concentrations vary with time in a nonparallel fashion.

4.4. Comparison with Experimental Data. The data in Figure 7 were used to evaluate the effective dimer segregation coefficient as defined in eqs 17–19. The resulting values for the two types of mass transport are shown in Table 1 together with experimental data from growth of ferritin crystals aboard the space shuttle during the STS 95 mission and their ground controls¹⁰ and in later experiments.³⁷ The sets of values resulting from the model are close to the experimental data. The somewhat higher impurity incorporation from ground-based experiments is likely caused by vibrations and other impacts in the laboratory that enhance stirring and impurity supply to the growth interface. Still, the relatively good correspondence between the model and experimental results suggest that suppression of buoyancy-driven convection may lead to lower impurity incorporation and, hence, to better crystal quality.

Acknowledgment. This work would not have been possible without constant interactions with A. A. Chernov and D. C. Carter, who also provided access to unpublished results of space- and ground-based experiments. L. Carver expertly prepared the figures. This research was supported by the Office of Life and Microgravity Sciences and Applications of NASA (Grants NAG8-1354 and 97-HEDS 02-50) and the National Heart, Lung and Blood Institute, NIH (Grant HL 58038).

References

- Burley, S. K.; Almo, S. C.; Bonanno, J. B.; Capel, M.; Chance, M. R.; Gaasterland, T.; Lin, D.; Sali, A.; Studier, F. W.; Swaminathan, S. *Nat. Genet.* **1999**, *23*, 151–157.
- McPherson, A. *Crystallization of Biological Macromolecules*; Cold Spring Harbor Laboratory Press: Cold Spring Harbor, NY, 1999.
- Giege, R.; Lorber, B.; Theobald-Dietrich, A. *Acta Crystallogr., Sect. D* **1994**, *50*, 339–350.
- McPherson, A.; Malkin, A. J.; Kuznetsov, Y. G.; Koszelak, S. *J. Cryst. Growth* **1996**, *168*, 74–92.
- Chernov, A. A. *J. Cryst. Growth* **1999**, *196*, 524–534.
- Ferre-D-Amare, A. R.; Burley, S. K. *Structure* **1994**, *15*, 357–359.
- Thomas, B. R.; Vekilov, P. G.; Rosenberger, F. *Acta Crystallogr., Sect. D* **1996**, *52*, 776–784.
- Thomas, B. R.; Carter, D.; Rosenberger, F. *J. Cryst. Growth* **1997**, *187*, 499–510.
- Yoon, T.-S.; Tetreault, S.; Bosshard, H. E.; Sweet, R. M.; Sygush, J. *J. Cryst. Growth*, in press.
- Thomas, B. R.; Chernov, A. A.; Vekilov, P. G.; Carter, D. C. *J. Cryst. Growth* **2000**, *211*, 149–156.
- Pusey, M.; Witherow, W.; Naumann, R. *J. Cryst. Growth* **1988**, *90*, 105–111.
- Lin, H.; Rosenberger, F.; Alexander, J. I. D.; Nadarajah, A. *J. Cryst. Growth* **1995**, *151*, 153–162.
- Vekilov, P. G.; Thomas, B. R.; Rosenberger, F. *J. Phys. Chem.* **1998**, *102*, 5208–5216.
- Vekilov, P. G.; Rosenberger, F. *Phys. Rev. E* **1998**, *57*, 6979–6981.
- Rosenberger, F.; Vekilov, P. G.; Muschol, M.; Thomas, B. R. *J. Cryst. Growth* **1996**, *167*, 1–27.
- Carter, D. C.; Lim, K.; Ho, J. X.; Wright, B. S.; Twigg, P. D.; Miller, T. Y.; Chapman, J.; Keeling, K.; Ruble, J.; Vekilov, P. G.; Thomas, B. R.; Rosenberger, F.; Chernov, A. A. *J. Cryst. Growth* **1999**, *196*, 623–637.
- Vidal, O.; Robert, M. C.; Bouie, F. *J. Cryst. Growth* **1998**, *192*, 257–270.
- Frank, F. C. In *Growth and Perfection of Crystals*; Doremus, R. H., Roberts, B. W., Turnbull, D., Eds.; Wiley: New York, 1958; pp 411–417.
- Caylor, C. L.; Dobrianov, I.; Lemay, S. G.; Kimmer, C.; Kriminski, S.; Finkelstein, K. D.; Zipfler, W.; Webb, W. W.; Thomas, B. R.; Chernov, A. A.; Thorne, R. E. *Proteins: Struct., Funct., Genet.* **1999**, *36*, 270–281.
- Ramachandran, N.; Baugher, C. R.; Naumann, R. J. *J. Cryst. Growth* **1995**, *8*, 170–179.
- Lin, H.; Vekilov, P. G.; Rosenberger, F. *J. Cryst. Growth* **1996**, *158*, 552–559.
- Massover, W. H. *Micron* **1993**, *24*, 389–437.
- Harrison, P. M.; Arosio, P. *Biochim. Biophys. Acta* **1996**, *1275*, 161–203.
- Petsev, D. N.; Thomas, B. R.; Yau, S.-T.; Vekilov, P. G. *Biophys. J.* **2000**, *78*, 2060–2069.
- Yau, S.-T.; Thomas, B. R.; Vekilov, P. G. Submitted for publication in *Proteins: Struct., Funct., Genet.*
- Yau, S.-T.; Thomas, B. R.; Vekilov, P. G. *Phys. Rev. Lett.* **2000**, *85*, 353–356.
- Carter, D. C.; Wright, B. S.; Miller, T. Y.; Chapman, J.; Twigg, P. D.; Keeling, K.; Moody, K.; White, M.; Click, J.; Ruble, J.; Ho, J. X.; Adhock-Downeey, L.; Bunick, G.; Harp, J. *J. Cryst. Growth* **1999**, *196*, 602–609.
- Vekilov, P. G.; Lin, H.; Rosenberger, F. *Phys. Rev. E* **1997**, *55*, 3202–3214.
- Rosenberger, F.; Lin, H.; Vekilov, P. G. *Phys. Rev. E* **1999**, *59*, 3155–3164.
- Lawson, D. M.; Artymiuk, P. J.; Yewdall, S. J.; Smith, J. M. A.; Livingstone, J. C.; Trefry, A.; Luzzago, A.; Levi, S.; Arosio, P.; Cesareni, G.; Thomas, C. D.; Shaw, W. V.; Harrison, P. M. *Nature* **1991**, *349*, 541–544.
- Hempstead, P. D.; Yewdall, S. J.; Fernie, A. R.; Lawson, D. M.; Artymiuk, P. J.; Rice, D. W.; Ford, G. C.; Harrison, P. M. *J. Mol. Biol.* **1997**, *268*, 424–448.
- Chernov, A. A. *Modern Crystallography III: Growth of Crystals*; Springer: Berlin, 1984.
- Chernov, A. A. *Contemp. Phys.* **1989**, *30*, 251–276.
- Vekilov, P. G.; Monaco, L. A.; Rosenberger, F. *J. Cryst. Growth* **1995**, *156*, 267–278.
- Vekilov, P. G.; Rosenberger, F. *J. Cryst. Growth* **1996**, *158*, 540–551.
- Yau, S.-T. Unpublished data.
- Thomas, B. R. Unpublished results.
- Lin, H. Unpublished data.

CG005515G